

### Calibration of Near-Infrared Passive Radiometry from the Lunar Orbiter Laser Altimeter (LOLA).

R. T. Walker<sup>1,2</sup>, M. K. Barker<sup>1</sup>, X. Sun<sup>1</sup>, E. Mazarico<sup>1</sup>, D. E. Smith<sup>3</sup>, M. T. Zuber<sup>3</sup>, and G. A. Neumann<sup>1</sup>.

<sup>1</sup>Solar System Exploration Division, NASA Goddard Space Flight Center, 8800 Greenbelt Rd., Greenbelt, MD 20771 (ryan.t.walker@nasa.gov), <sup>2</sup>Hexagon US Federal, 4600 Forbes Blvd, Lanham, MD 20706, <sup>3</sup>Dept. of Earth, Atmospheric and Planetary Sciences, MIT, 77 Massachusetts Ave., Cambridge, MA 02139.

**Introduction:** The reflectance of the lunar surface across a range of wavelengths and viewing geometries can reveal important geological and physical properties of the regolith. When not in altimetry mode, the Lunar Orbiter Laser Altimeter (LOLA) aboard the Lunar Reconnaissance Orbiter (LRO) can be operated as a 4-channel near-infrared (1064 nm) passive radiometer [1]. With the laser inactive, the threshold and gain of the detectors are adjusted so that the solar photons reflected off the lunar surface that are “noise” for altimetry become the signal. The raw data are collected at a rate of 28 Hz, and the combined footprint of all channels has a diameter of  $\sim 120$  m from 100 km altitude. Before observations can be analyzed, the raw data must be calibrated to account for time- and temperature-dependent characteristics of the individual detectors and converted from photon counts to absolute radiance. Here, we derive the global photometric and phase functions from data collected from Dec. 2013 (the start of passive radiometry) through Dec. 2020.

**Methods:** We begin with the raw photon (noise) counts from 4 of LOLA’s 5 detector channels. (Channel 1, corresponding to the central spot of the footprint, is not used for passive radiometry because it also receives photons from the laser ranging telescope mounted on the high-gain antenna.) The calibration also requires the

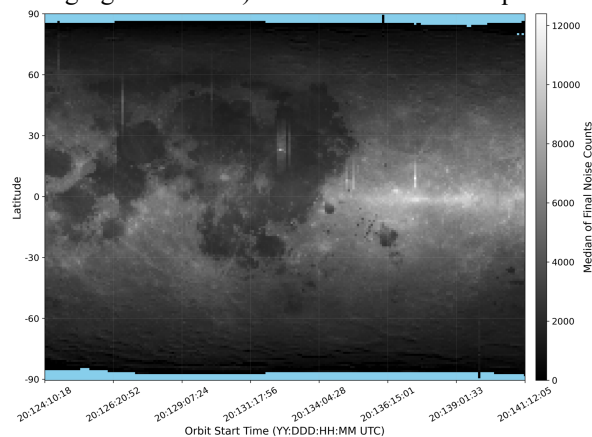


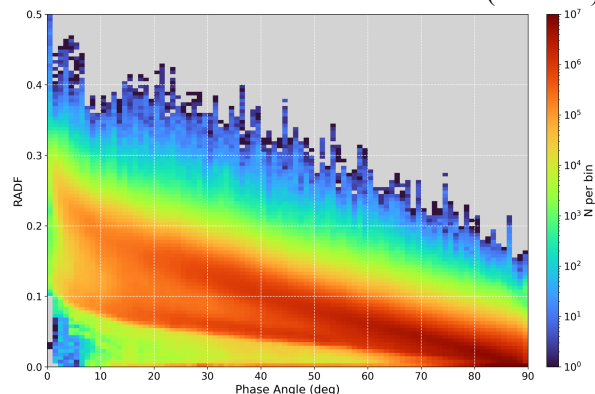
**Figure 1:** Sample ( $\sim 3$  May 2020–20 May 2020) of final normalized LOLA photon counts, shown as the median over  $1^\circ$  latitude bins. Each orbit is one column. The bright strip along the equator is caused by the opposition effect, in which the intensity sharply increases approaching zero phase due to coherent backscatter and/or the reduction of shadow hiding [4].

viewing geometry: the incidence angle ( $i$ ) is the angle between the surface normal and surface-to-Sun vectors, the emission angle ( $e$ ) is the angle between the surface normal and surface-to-observer vectors, and the phase angle ( $g$ ) is the angle between the surface-to-Sun and surface-to-observer vectors. We calculate these angles using the Embree ray-tracing package, SPICE toolkit from the Jet Propulsion Laboratory, and the LOLA 128 pix/deg shape model. The calibration then follows the steps described in [1], which calibrated the first  $\sim 1$  year of LOLA passive radiometry.

**Dark current.** Even without incident light, thermal electrons in the detectors cause nonzero noise counts. We fit this dark current (raw night noise counts) with a cubic function of time and detector temperature and subtract the result from the raw day noise counts. The RMS residual across all channels is  $\sim 60 - 70$  counts, and the dark current increases by  $\sim 2 - 3\%$  per year.

**Responsivity.** Each detector responds differently to the same level of incident light. We fit the ratios between detectors of dark-subtracted day noise counts with a cubic function of time and temperature and use this fit to normalize the counts relative to Channel 3. (We choose Channel 3 as the reference for consistency with [1].) The RMS residual is  $\sim 10\%$ , and the responsivities increase by  $\sim 1 - 2\%$  per year.

**Reference channel trend.** The response of Channel 3 to incident light changes over time. We extract a photometrically uniform subset of the data and calculate the variation in counts relative to the median (as a ratio)



for observations with similar viewing geometry and

**Figure 2:** Radiance factor (RADF), shown in  $1^\circ \times 0.005$  bins. Two branches are visible at low phase angles, due to the high albedo of the highlands (upper branch) relative to the maria (lower branch).

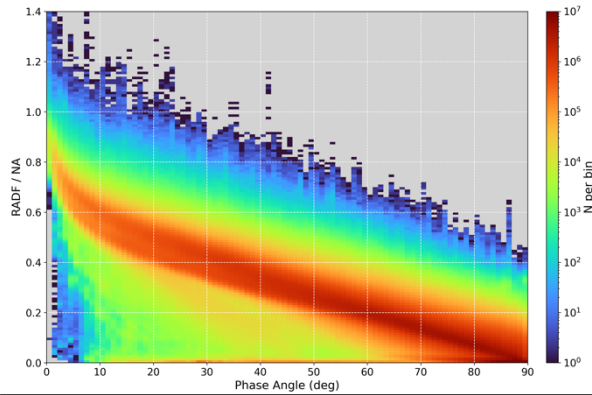


**Figure 3:** Photometric function, shown in  $1^\circ \times 0.01$  bins. This removes most of the albedo-dependence of the RADF. The small remaining difference in photometric function of highlands and maria is due to other factors influencing RADF besides albedo, such as opposition effect, single particle phase function, and roughness [1].

albedo using  $1^\circ \times 1^\circ \times 1^\circ$  bins of  $i$ ,  $e$ ,  $g$  and a subsample with 1064 nm normal albedo 0.25 – 0.35 [5]. We then fit a cubic function of time and use it to derive a final corrected noise count (mean across 4 channels) for each observation (Fig. 1). The RMS residual of the fit is  $\sim 20\%$ , and the ratio decreases by  $\sim 2\%$  per year.

**Absolute radiance.** In these preliminary results [3], we use the linear calibration of [1], to convert the normalized noise counts, which are specific to LOLA, to absolute radiance  $I_0(i, e, g)$  by comparison with the SELENE (Kaguya) Spectral Profiler dataset. We are currently working on an updated calibration using the  $\sim 7$  years of observations analyzed in this study.

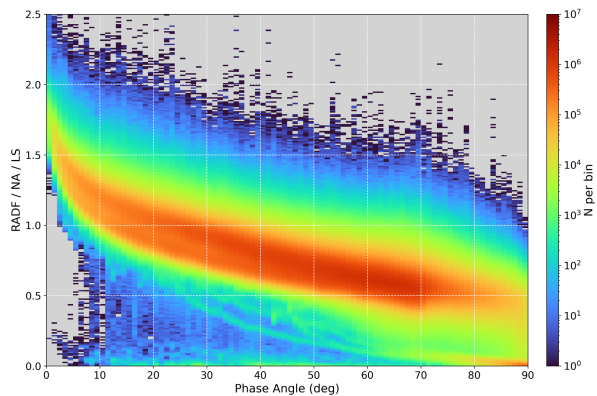


**Figure 4:** Phase function, shown in  $1^\circ \times 0.01$  bins, summed over incidence angles  $< 70^\circ$  and all emission angles. This approximately corrects for topography assuming a Lommel-Seeliger law. We include only data with  $i < 70^\circ$  to mitigate the effects of shadows and errors in the topographic correction.

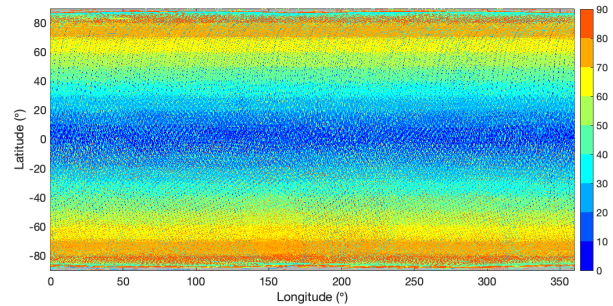


**Figure 5:** Minimum phase angle for all passive radiometry observations, calculated over  $0.0625^\circ \times 0.0625^\circ$  longitude-latitude bins ( $\sim 2$  km at the equator).

The radiance factor (RADF; Fig. 2), also called I/F, is defined as reflectance relative to a perfectly diffuse (Lambertian) surface illuminated vertically:  $RADF(i, e, g) = \pi I_0(i, e, g) / J_0 \times D^2$ , where  $J_0 = 647 \text{ W/m}^2/\mu\text{m}$  is the solar irradiance at 1064 nm at 1 AU, and  $D$  is the Sun-Moon distance in AU [4]. The photometric function (Fig. 3), derived by dividing RADF by the normal albedo  $A_n$  (using the global map from [5]), contains all illumination and viewing geometry effects. The photometric function can be separated into a limb-darkening function depending only on  $(i, e)$  and a phase function depending only on  $g$  [4]. Using the Lommel-Seeliger law  $LS(i, e) = \cos(i) / (\cos(i) + \cos(e))$ , the phase function (Fig. 4) is  $\Phi(g) = RADF(i, e, g) / A_n / LS(i, e)$ .

**Summary:** The  $\sim 7$  years of data presented here provide greater phase angle and spatial coverage compared to the first year of data [1] due to the evolution of LRO's orbit over this time period. However, additional phase coverage is needed especially at low phase angles and local scales for small ( $< \sim 10$  km), high-value science targets at mid-to-high latitudes (Fig. 5). This will require targeted spacecraft slews in the future given LRO's nadir-pointing geometry. The data will be analyzed to provide new insights about the global, regional, and local scattering properties of the lunar surface. These measurements are complementary to the ultraviolet-visible reflectance measurements made by the LRO Camera (LROC) and Lyman-Alpha Mapping Project (LAMP) instruments since they allow the same phase function characterization and identification of photometric anomalies [1,2,6].

**References:** [1] Barker, M. K. et al. (2016) *Icarus*, 273, 96. [2] Sato, H. et al. (2014) *JGR Planets*, 119, 1775. [3] Walker, R. T. et al. (2021) *AGU Fall Meeting*, Abstract #947705. [4] Hapke, B. (2012) Camb. Univ. Press, *Theory of Refl. and Emitt. Spect.*, 2nd ed. [5] Lemelin, M. et al. (2016) *Icarus*, 273, 315. [6] Liu, Y. (2018) *JGR Planets*, 123, 2550.